Opto-Electronic Advances

ISSN 2096-4579 CN 51-1781/TN

Strong coupling and catenary field enhancement in the hybrid plasmonic metamaterial cavity and TMDC monolayers

Andergachew Mekonnen Berhe, Khalil As'ham, Ibrahim Al-Ani, Haroldo T. Hattori and Andrey E. Miroshnichenko

Citation: Berhe AM, As'ham K, Al-Ani I, et al. Strong coupling and catenary field enhancement in the hybrid plasmonic metamaterial cavity and TMDC monolayers. *Opto-Electron Adv* **7**, 230181(2024).

https://doi.org/10.29026/oea.2024.230181

Received: 30 September 2023; Accepted: 19 December 2023; Published online: 31 January 2024

Opto-Electronic Advances

Article

May 2024, Vol. 7, No. 5

DOI: 10.29026/oea.2024.230181

Strong coupling and catenary field enhancement in the hybrid plasmonic metamaterial cavity and TMDC monolayers

Andergachew Mekonnen Berhe, Khalil As'ham, Ibrahim Al-Ani, Haroldo T. Hattori and Andrey E. Miroshnichenko*

Strong coupling between resonantly matched surface plasmons of metals and excitons of quantum emitters results in the formation of new plasmon-exciton hybridized energy states. In plasmon-exciton strong coupling, plasmonic nanocavities play a significant role due to their ability to confine light in an ultrasmall volume. Additionally, two-dimensional transition metal dichalcogenides (TMDCs) have a significant exciton binding energy and remain stable at ambient conditions, making them an excellent alternative for investigating light-matter interactions. As a result, strong plasmon-exciton coupling has been reported by introducing a single metallic cavity. However, single nanoparticles have lower spatial confinement of electromagnetic fields and limited tunability to match the excitonic resonance. Here, we introduce the concept of catenary-shaped optical fields induced by plasmonic metamaterial cavities to scale the strength of plasmon-exciton coupling. The demonstrated plasmon modes of metallic metamaterial cavities offer high confinement and tunability and can match with the excitons of TMDCs to exhibit a strong coupling regime by tuning either the size of the cavity gap or thickness. The calculated Rabi splitting of Au-$MoSe_2$ and Au-WSe_2 heterostructures strongly depends on the catenary-like field enhancement induced by the Au cavity, resulting in room-temperature Rabi splitting ranging between 77.86 and 320 meV. These plasmonic metamaterial cavities can pave the way for manipulating excitons in TMDCs and operating active nanophotonic devices at ambient temperature.

Keywords: catenary-shaped field enhancement; strong coupling; plasmon; exciton; Rabi splitting

Berhe AM, As'ham K, Al-Ani I et al. Strong coupling and catenary field enhancement in the hybrid plasmonic metamaterial cavity and TMDC monolayers. *Opto-Electron Adv* **7**, 230181 (2024).

Introduction

An optical cavity can control and confine electromagnetic fields, inducing enhanced light-matter interactions at the nanoscale. Recently, researchers have dedicated significant effort to plasmon-exciton coupling, which is based on the strong coupling of plasmons in metallic nanomaterials with excitons in quantum emitters to develop advanced nanophotonic devices[1–4]. When the plasmon resonance in a metallic cavity strongly couples with semiconductor excitons, a new mixed state known as a plexciton is formed. Such strong coupling can be achieved when the energy exchange rates between these subsystems are faster than the decay rates of the plasmons and excitons[5]. This regime promotes the formation of hybrid states that are part-light and part-matter, which is crucial for realizing nanophotonic devices that can surpass the speed of semiconductor electronics and the size limitations of photonic dielectrics[6]. The

School of Engineering and Technology, University of New South Wales at Canberra, Northcott Drive, Canberra ACT 2610, Australia.
*Correspondence: AE Miroshnichenko, E-mail: andrey.miroshnichenko@unsw.edu.au
Received: 30 September 2023; Accepted: 19 December 2023; Published online: 31 January 2024

coupling strength of the system can be enhanced by high-quality plasmonic cavities. To elucidate the presence of energy exchange between plasmons and excitons, plasmonic nanocavities play a significant role due to their tunability and their ability to confine light in an ultrasmall volume[7]. Hence, by decreasing the effective cavity volume (V), interaction times can be boosted, and the round trip for photons to return to the same emitter increases the coupling, which scales as $g \propto 1/\sqrt{V}$, where g is the coupling energy[7,8].

Several groups have reported strong coupling between plasmons in metallic nanoantenna and excitons in quantum emitters such as J-aggregates[9], molecules[10], or quantum dots (QD) semiconductors[3]. However, a substantial number of organic molecules must be included to achieve strong coupling in molecular excitons. Because the coupling strength increases with increasing emitter numbers, $g \propto \sqrt{N}$ is involved in the system[11]. Moreover, controlling the electric field confinement around the plasmonic cavity is challenging[12]. Compared to QD semiconductors, TMDC monolayers are stable at ambient conditions, making them excellent candidates to observe plasmon-exciton coupling. Furthermore, TMDC monolayers have large exciton binding energies with sharp exciton resonances, making them excellent candidates for light–matter studies and beyond[13–15]. Consequently, the plasmon modes of individual nanoparticles such as Au nanorods[16], silver (Ag) nanorods[11], and Ag nanodisks[12] demonstrated a strong coupling criterion with TMDCs as excitonic modes. In the strong coupling of plexcitons, active control of an individual metal nanoparticle should be demonstrated. Zheng et al. realized the strong coupling of surface plasmon on an individual Ag nanorod with excitons in a tungsten diselenide (WSe_2) monolayer. However, this strong coupling was achieved by depositing different thicknesses of alumina to produce plasmon–exciton detuning, which is not reversible with the plasmonic scanning method[11,17]. Moreover, XB Han et al. demonstrated the strong coupling of a plexciton system formed by randomly spraying silver nanocubes onto the tungsten disulfide (WS_2) monolayer[18]. However, randomly sprayed nanoparticles may not be suitable for integrating complex systems.

To address this issue, we investigated a strong coupling of surface plasmons on metallic metamaterial nanocavities with excitons in TMDC monolayers. This metallic metamaterial nanocavity was introduced by transforming surface plasmon polaritons (SPP) with strong near-field enhancement rather than directly coupling to Localized Surface Plasmon Resonance (LSPR)[19]. The introduced plasmonic metamaterial nanocavity, hereafter referred to as the Au/Ag cavity, exhibits catenary-shaped optical fields[20]. These catenary-shaped optical fields in metal-dielectric-metal (MIM) structures can be formed by coupling of surface plasmons in the cavity[21]. The strength of this catenary-shaped electric field distribution is strongly dependent on the cavity's gap. Recently, YJ Huang et al. introduced the concept of catenary electromagnetic field theory to manipulate electromagnetic wave properties in metallic slits and confirmed that the electric field distribution in metallic slits takes the form of hyperbolic cosine function. The catenary-shaped optical field induced by the metallic slit also strongly depends on the slit's gap width[22]. In line with metallic slits, the electromagnetic properties in metallic grating follow a hyperbolic cosine shape, as the scattering fields at the interface of the MIM structure are primarily evanescent waves. The catenary-shaped field distribution induced by the metallic gratings decreases with increasing gap widths[23]. Therefore, controlling the cavity gap in metallic metamaterials/nanoantennas is crucial for managing the electric field confinement. Thus, higher field confinement in plasmonic cavities is a necessary condition for enhancing light-matter interactions. To the best of our knowledge, the strong coupling between TMDC monolayer excitons and a plasmonic mode of a metallic metamaterial cavity has not been investigated.

Here, active control in the Au/Ag cavity tunes the plasmon resonance frequency, allowing the plasmon mode to match with the excitons of TMDC monolayers. By adjusting the cavity gap and the thickness of the nanostructures, the plasmon resonances of Au/Ag cavities align with the excitons of WSe_2, molybdenum diselenide ($MoSe_2$), and WS_2 monolayers. Moreover, the proposed design involves a complex nanocavity with plasmon coupling properties, resulting in greater field enhancement and exhibiting striking properties, such as plasmon hybridization, which is crucial for investigations into strong coupling[18]. Consequently, this article mainly focuses on the Au cavity as the plasmon mode and $MoSe_2$ and WSe_2 as the exciton modes. It is found that plexciton energies can be realized by varying the cavity gap and the thickness of the gold nanostructures. Therefore, a large Rabi splitting ranging from 77.86 and 320 meV is achieved by Au-$MoSe_2$ and Au-WSe_2

heterostructures based on highly localized field enhancement in the near field of Au cavity. The proposed heterostructures will improve the understanding of the advantages of catenary-shaped optical fields in scaling the Rabi splitting of plexcitons. Moreover, this strong light-matter coupling with a large Rabi splitting has the potential to enable the realization of a single-photon emitter by enhancing spontaneous emission. Besides, the designed plasmonic metamaterial cavity has relatively higher *Q*-factor and can sustain electromagnetic fields for longer durations with lower energy losses. Furthermore, the enhanced interaction between the plasmon–excitons leads to the realization of compact and low-threshold laser[24,25]. This advancement also applies to the development of optoelectronic devices, optical switching, and sensing[26–28].

Results and discussion

The schematic structure shown in Fig. 1(a) demonstrates an Au cavity, designed to tune the plasmon resonances. Au/Ag cavities are employed as plasmon modes and WSe_2, $MoSe_2$, and WS_2 monolayers are used as exciton modes. It is important to note that Au–$MoSe_2$ and Au–WSe_2 heterostructures were specifically investigated to validate the presence of strong coupling under ambient conditions. The transmission, reflection, and absorption spectra of the uncoupled WSe_2, $MoSe_2$, and WS_2 were first calculated using Rigorous Coupled-Wave Analysis (RCWA). Their thickness was assumed to be 0.7 nm, and their in-plane permittivity was modelled using the Lorentz oscillator[29]:

$$\varepsilon(E) = \varepsilon_{\mathrm{B}} + \frac{f}{E_{\mathrm{exciton}}^2 - E^2 - \mathrm{i}\Gamma E}, \tag{1}$$

where f is the oscillator strength, ε_{B} is the background dielectric constant, E_{exciton} is the exciton energy, and Γ is the width of the excitons. The optical values of WSe_2, $MoSe_2$, and WS_2 monolayers were taken from Ibrahim A. M. *et al.*[30] and consecutive results were taken for Rabi splitting calculations. Additionally, the permittivities of Au and Ag were obtained from the published data of Johnson and Christy[31]. Then, numerical simulations of the electromagnetic properties of the hybrid nanostructures were performed using Finite-Difference Time-Domain (FDTD) Solutions (by Lumerical, Inc.) with periodic boundary conditions along the x and y directions and perfectly matched layers (PML) in the z-direction. A plane wave source with normal incidence along the z-direction and a wavelength ranging from 600 nm to 900 nm was used as the light source.

A predetermined condition must be met to systematically investigate the plasmon-exciton coupling in Au-$MoSe_2$ and Au-WSe_2 heterostructures and verify the tunability of the plasmon resonance of the Au cavity. As shown in Fig. 1(b), the absorption mapping depicts the tunability of plasmon resonances of the Au cavity by varying its thickness from 20 nm to 120 nm. Its absorption peaks shifted from 822 nm to 687 nm with increasing thickness. Figure 1(c) illustrates that the plasmon resonance of the uncoupled Au cavity with a thickness of 60 nm overlaps with the exciton energy of the WSe_2 monolayer. This design, which features tunable plasmon resonance and a strong catenary-shaped near-field enhancement, involves controlling the local electromagnetic field distribution near the surface of the Au cavity. Figure 1(d) and 1(e) show the induced electric field profiles resulting from the strong interaction between light and free electrons in gold. As revealed in Fig. 1(f), the Au cavity produces a catenary-shaped electric field profile at an air–gold interface[21]. This catenary-shaped optical field determines the thickness- and gap-dependent local field enhancement, which can be reduced with increasing thickness of the nanostructure. This size-dependent near-field enhancement plays a crucial role in studying the strong coupling.

Furthermore, the appropriately designed Au cavity is tunable concerning the polarization angle. Figure 1(g) reveals polarization-sensitive surface plasmon resonance (SPR) in the visible and near-infrared wavelengths. The plasmon resonance frequency of the Au cavity shifted to higher energy as the polarisation angle increased from 0° to 90° due to a gradual decrease in the TM mode while increasing the TE mode. Additionally, Fig. 1(h) shows that the near-field enhancement $|\boldsymbol{E}/\boldsymbol{E}_0|$ of the Au cavity is higher at 90° than that of 0°, which has tremendous implications for further strong coupling investigations. Besides, to demonstrate the effect of polarization angle on near-field enhancement at two different resonance energies, 0° and 45° are demonstrated in Fig. S1(a) and S1(b) in the Supplementary information. For a given excitation wavelength of λ = 859 nm, the TM mode (polarization along the x-axis) exhibits a higher near-field enhancement $|\boldsymbol{E}/\boldsymbol{E}_0|$ of 20.3 compared to 45° with 16.4, which has both TE and TM components. Conversely, as the polarization angle increases from 0° to 45°, the TM mode's absorbance and near-field enhancement $|\boldsymbol{E}/\boldsymbol{E}_0|$ decrease simultaneously due to the increasing TE mode.

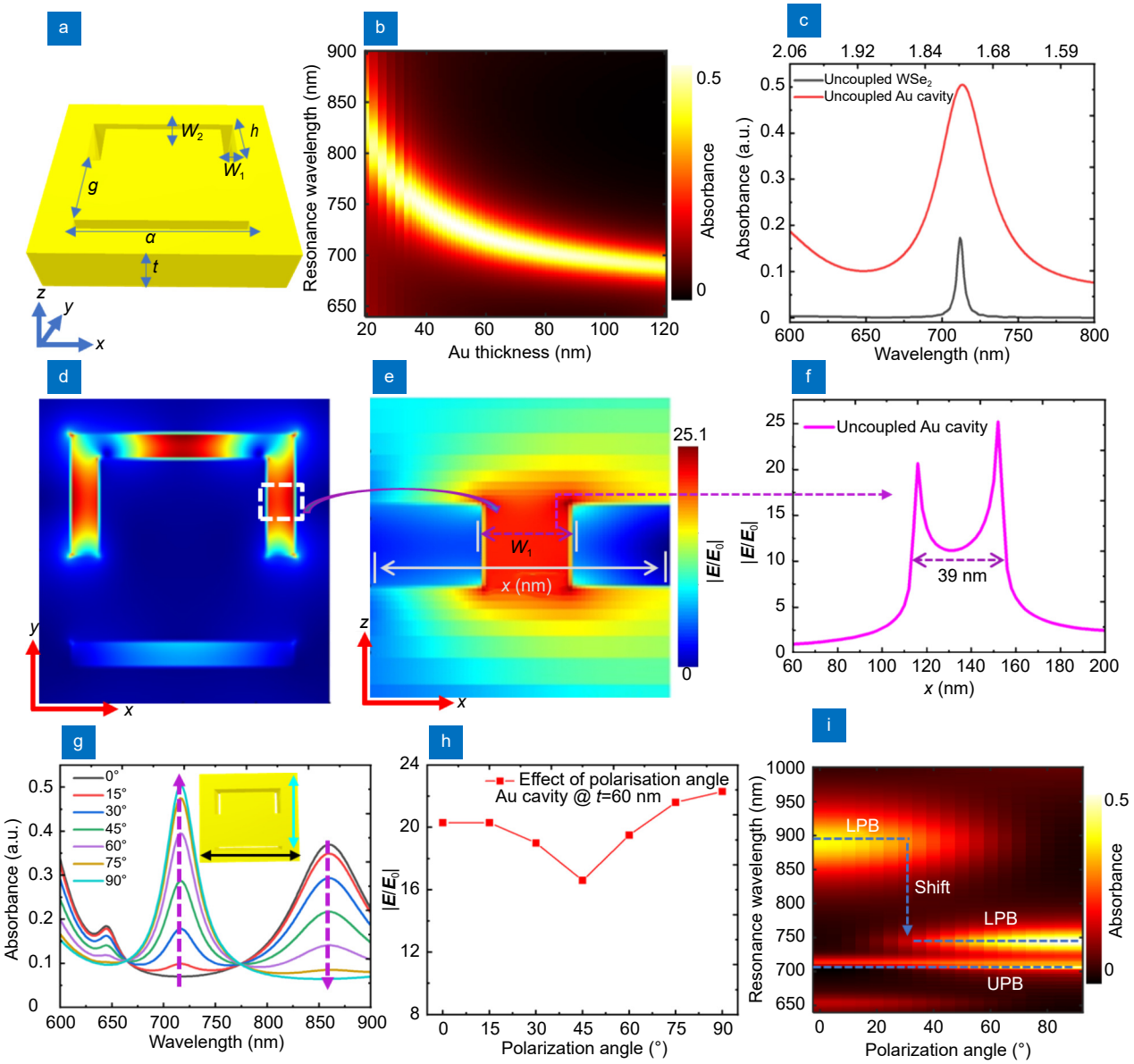

Fig. 1 | Plasmon resonances and electric field distribution in Au cavity. (**a**) Schematic drawing of Au nanostructure with design parameters of the structure are as follows: W_1 = 39 nm, W_2 = 33 nm, h =157 nm, g = 108 nm, α = 307 nm, and t = 60 nm. (**b**) Absorption mapping of uncoupled Au cavity at a p = 420 nm period. (**c**) The absorbance of uncoupled Au cavity (red line) and the uncoupled WSe_2 monolayers. The Au cavity's resonance wavelength is designed to resonate with the exciton in WSe_2. The electric field is generated at a unit cell of the Au cavity, at the planes (**d**) z = 13 nm and (**e**) y = 70 nm with a polarization along the y-axis. (**f**) The retrieved catenary-shaped near-field enhancement at air−gold interfaces. (**g**) The absorption spectra of the Au cavity at different polarisation angles. The thickness of the Au cavity gap was fixed at 60 nm with cavity gaps of W_1 = 39 nm and W_2 = 33 nm. The polarization angle of 0° is along the x-axis, and 90° is along the y-axis. (**h**) Near-field enhancement $|\boldsymbol{E}/\boldsymbol{E}_0|$ with increasing polarisation angle from 0° − 90°. (see (e) for the position). (**i**) The absorption mapping of Au-WSe_2 heterostructure at different polarization angles.

Hence, for an excitation wavelength of λ = 716 nm, the near-field enhancement increases from 3.89 to 15.9 with increasing polarization angle from 0° to 45° (see Fig. S1(a) and S1(b) in the Supplementary information). Moreover, the plasmon absorbance band at a polarization angle of 0° (TM mode) is out of phase with that of 90° (TE mode), which induces a tunable Fano resonance[32]. Additionally, to demonstrate the effect of the period on tuning plasmon resonance of the Au cavity, we have performed simulations, as shown in Fig. S2 in the Supplementary information. The period's effect in tuning the plasmon resonance is found to be almost negligible.

After confirming the tunability of the plasmon

resonance of the uncoupled Au cavity, we also investigated the polarization-dependent absorption spectrum of the Au-WSe_2 heterostructure. Figure 1(i) shows the absorption spectrum of the Au-WSe_2 hybrid nanostructure, with the lower plexciton branch (LPB) blueshifting with increasing polarization angle while the upper plexciton branch (UPB) remains positioned at the WSe_2 exciton resonances. This indicates the polarization insensitivity of Rabi splitting. Furthermore, the TE mode induces a higher electric field enhancement in the cavity, making it the choice for further strong coupling studies.

The interaction between excitons of TMDCs and the plasmon modes of the Au cavity can be continuously tuned by adjusting the size of the Au nanostructure. This led us to investigate the presence of strong coupling. Figure 2(a) and 2(d) present the sketched nanostructures of the plasmonic Au cavity combined with $MoSe_2$ and WSe_2 monolayers, respectively. Their corresponding energy resonances (see Fig. 2(b) and 2(e)) reveal that the plasmon-exciton coupling strength can be effectively tuned by varying the Au thickness. The LPB blueshifts with increasing Au thickness and approaches the excitons of $MoSe_2$ and/or WSe_2, while the UPB shifts away from the excitons. Hence, the absorption spectrum shows two distinct peaks energetically shifted from the uncoupled plasmon and exciton resonances (see Fig. 2(c) and 2(f)), indicating the presence of new eigenstates. This confirms the formation of plexciton states in the hybrid nanostructures. The frequency splitting implies a coherent exchange of energy between the plasmon and the exciton modes[33]. Additionally, as shown in Fig. 2(g–i), in comparison with the pure plasmon mode of the Au cavity, Au-WSe_2 heterostructures exhibit a higher electric field enhancement, providing faster energy exchange in the hybrid system.

It's worth noting that the difference in absorbance between the uncoupled Au cavity, shown in Fig. 1(c), and the coupled heterostructures in Fig. 2(c) and 2(f), might arise due to the cavity gap width. As illustrated in Fig. S3(a) of the Supplementary information, the Au-WSe_2 heterostructure exhibits higher absorbance than the uncoupled Au cavity. However, the near-field enhancement $|\boldsymbol{E}/\boldsymbol{E}_0|$ decreases from 98.3 to 39.8 with increasing the cavity gap (W_1) increases from 39 nm to 59 nm (refer to Figs. 2(h) and S3(c) in the Supplementary information). Generally, for such complex geometries, comparing absorbance and electric field enhancement directly is not feasible. This is because absorbance represents the total integration of electromagnetics over the entire structure, while electric field enhancement is measured at specific cavity locations and varies across different points, as shown in Fig. S3(b) and S3(c) in the Supplementary information.

Moreover, the demonstrated electric field distribution in Fig. 2(i) is modelled using the rigorous catenary model[22].

$$E\left(x\right) = a \cdot \cosh\left(bx\right) + c\ , \tag{2}$$

where, a, b, and c are fitting parameters that determine the shape of the catenary curve. As can be seen from Fig. 1(a), the designed Au cavity has a complex structure, and can induce multiple catenary-shaped field response. As a result, Eq. (2) can be deduced to the form:

$$E\left(x\right) = a \cdot \cosh\left(b(x \pm k)\right) + c\ , \tag{3}$$

where, k is a horizontal translation factor, shifting the catenary curve left or right horizontally. The electric field distribution in Fig. 2(i) was extracted from the right side of Fig. 2(g), resulting in $+k$ (i.e., $x - k$), which indicates that the curve is shifted to the right by 133.949 units. Conversely, as shown in Fig. S4(b–left) in the Supplementary information, the extracted electric field distribution was from the left side of the z plane, resulting in $-k$ (i.e., $x + k$) which indicates that the curve is shifted to the left by −127.991 units. In both conditions, the near-field enhancement induced by the Au cavity and its corresponding hybrid structures follows the hyperbolic cosine function. This catenary-shaped optical field is strongly dependent on the gap width of the cavity, which is crucial to manipulate coupling strength between excitons of TMDC monolayers and plasmon of metamaterial cavities. As mentioned above the current design could demonstrate strong coupling between the Au cavity and TMDC monolayers.

The observed strong coupling of the Au-$MoSe_2$ and Au-WSe_2 heterostructures, dispersion curves of $MoSe_2$ and WSe_2 monolayers, uncoupled Au cavity, and their hybrid heterostructure are calculated by varying the cavity gap size and the thickness of the Au nanostructure. The strong coupling of Au-$MoSe_2$ and Au-WSe_2 as revealed in Fig. 2(c) and 2(f) has two distinct resonances: a higher energy mode (E_+) referred to as the UPB and a lower energy mode ($E\_$) referred to as the lower plexciton branch (LPB). The observed strong coupling of the hybrid nanostructure is shown in Fig. 3(a) and 3(c) were analysed using the coupled oscillator model:[34–36]

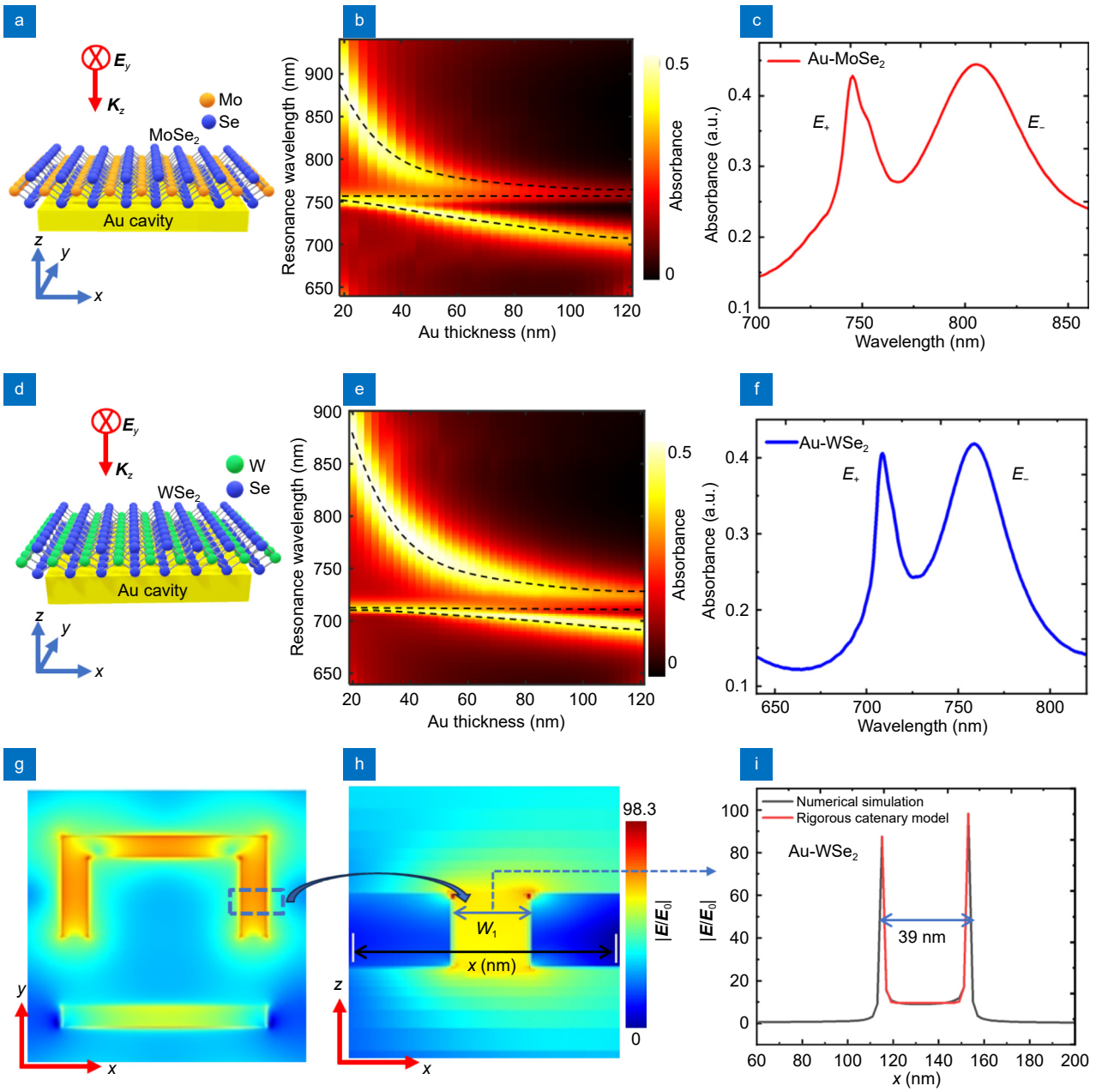

Fig. 2 | Catenary field enhancement and strong coupling in the Au-$MoSe_2$ and Au-WSe_2 heterostructure. (**a**) Schematic illustration of monolayer $MoSe_2$ on top of Au cavity at normal incidence. (**b**) Absorption spectrum mapping of Au-$MoSe_2$ as a function of the Au thickness varied from 20 to 120 nm while keeping other parameters constant (W_1 = 39 nm, W_2 = 33 nm, and period = 450 nm). Light is incident through TMDCs monolayers with polarisation along the *y*-axis. (**c**) The absorption spectrum of Au-$MoSe_2$ corresponds to (b) with a gold thickness of t = 36.6 nm. Two different hybridized modes, as the UPB (E_+), and LPB (E_-) are observed in absorption spectra. The demonstrated energy resonances were taken from the point of matching between excitons in $MoSe_2$ and the plasmon mode of the uncoupled Au cavity. (**d**) Schematic illustration of monolayer WSe_2 on top of Au cavity at normal incidence. (**e**) Absorption mapping of Au-WSe_2 heterostructures by tuning the thickness of Au nanostructure with a fixed value of W_1 = 39 nm, W_2 = 33 nm, h =157 nm, g = 108 nm, α = 307 nm, and p = 420 nm. (**f**) The absorption spectrum of Au-WSe_2 corresponds to (e) with a gold thickness of t = 60 nm. Electric field distribution at a unit cell of Au-WSe_2 nanostructure at the planes (**g**) *y*-plane and (**h**) *z*-plane using an excitation wavelength of 758 nm. (**i**) Catenary-shaped symmetric electric field profile of Au-WSe_2 with a cavity gap distance of W_1 = 39 nm. The magnitude of the electric field intensity distributions obtained by numerical simulations matched with the rigorous catenary model, where $a = 7.626\times10^{-9}$, b = −1.2529, k = 133.949, and c = 9.638 (see Eq. 3).

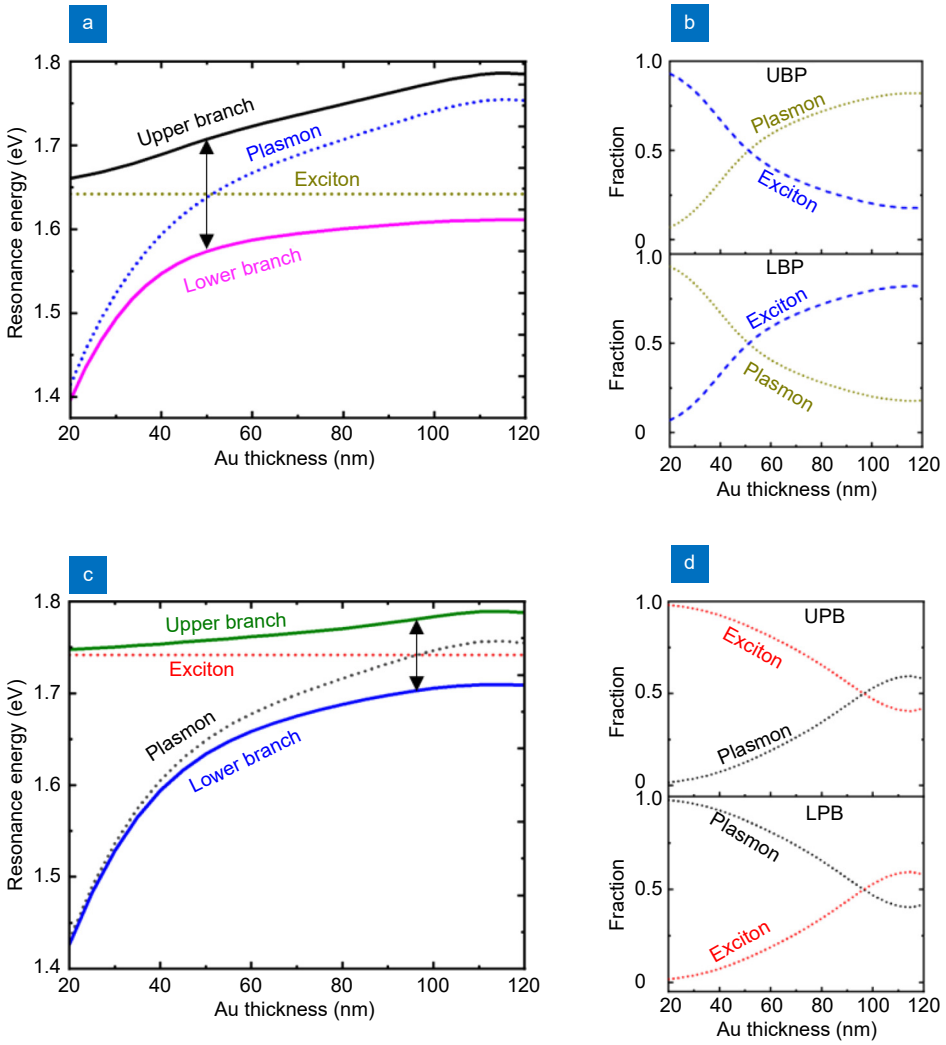

Fig. 3 | Anticrossing behaviour of the strong plasmon-exciton coupling of Au−$MoSe_2$ and Au−WSe_2 heterostructures. (**a**) Dispersion curve of Au−$MoSe_2$ heterostructure, where the solid black line, solid pink line, blue dash line, and olive dash line represent the UPB, LPB, uncoupled plasmon resonances, and uncoupled exciton resonances, respectively. (**b**) Hopfield coefficients for $MoSe_2$ exciton and plasmon contributions to UPB and LPB as a function of Au thickness. (**c**) Dispersion curve of Au−WSe_2 heterostructure, where the solid blue line, solid green line, black dash line, and red dash line represent the UPB, LPB, uncoupled plasmon resonances, and uncoupled WSe_2 exciton resonances. (**d**) Hopfield coefficients for WSe_2 exciton and plasmon contributions to UPB and LPB as a function of Au thickness.

$$\begin{pmatrix} E_{\rm P}+{\rm i}\hbar\Gamma_P & g_{\rm PX} \\ g_{\rm PX} & E_{\rm X}+{\rm i}\hbar\Gamma_{\rm X} \end{pmatrix}\begin{pmatrix} \alpha \\ \beta \end{pmatrix} = \boldsymbol{E}\begin{pmatrix} \alpha \\ \beta \end{pmatrix}, \quad (4)$$

where $E_{\rm P}$, and $E_{\rm X}$ are the resonance energies of the plasmon and exciton modes, $g_{\rm PX}$ is the coupling strength, and $\hbar\Gamma_{\rm P}$ and $\hbar\Gamma_{\rm X}$ are the half-widths at half-maximum (HWHM) of the plasmon and exciton modes. The eigenvalues E are the corresponding energies of the new quasiparticles, and α and β are eigenvector components of the upper and lower hybrid states that illustrate the intermixing behaviour and satisfy $|\alpha|^2+|\beta|^2=1$ depicted in Fig. 3(b) and 3(d). The eigenvalues E shown in Fig. 3(a) and 3(c) are also calculated as

$$E_{\pm} = \frac{1}{2}[(E_{\rm X}+E_{\rm P}])+{\rm i}(\hbar\Gamma_{\rm X}+\hbar\Gamma_{\rm P})] \pm\sqrt{g_{\rm PX}^2-\frac{1}{4}[E_{\rm X}-E_{\rm P}+{\rm i}\,(\hbar\Gamma_{\rm X}-\hbar\Gamma_{\rm P})]^2}, \quad (5)$$

The Rabi splitting ($\hbar\Omega_{\rm PX}$) of the plexciton is also extracted from the absorbance mapping data of Fig. 2(b) and 2(e) at the anticrossing point (detuning) where $E_{\rm P}=E_{\rm X}$, and Eq. (5) becomes:

$$\hbar\Omega_{PX}=2\sqrt{g_{PX}^2-\frac{1}{4}(\hbar\Gamma_X-\hbar\Gamma_P)^2}. \quad (6)$$

Additionally, it can be calculated by substituting the values of the HWHM of the uncoupled plasmon mode and uncoupled $MoSe_2$ and WSe_2 exciton modes.

Consequently, the Rabi splitting is extracted from the fitting of Fig. 3(a) and 3(c) for Au-$MoSe_2$ and Au-WSe_2, respectively. The calculated Rabi splitting for Au-$MoSe_2$ is 133.61 meV. In this calculation, the HWHM of $MoSe_2$ and WSe_2, as well as their exciton resonance, are assumed to remain constant throughout[37]. Subsequently, the coupling strength (g_{PX}) is calculated as

$$g_{PX} = \frac{\sqrt{\hbar\Omega_{PX}^2 + (\hbar\Gamma_P - \hbar\Gamma_X)^2}}{2}, \tag{7}$$

and it's 67.25 meV. Where, $\hbar\Gamma_P = 33.42$ meV, and $\hbar\Gamma_X = 16.05$ meV are HWHM of uncoupled Au cavity and $MoSe_2$ respectively. This coupling strength (g_{PX}) exceeds both the cavity loss rate, $\hbar\Gamma_P$, and the exciton scattering rate, $\hbar\Gamma_X$, resulting in energy cycling back and forth between matter and light components. Hence, to interact with light and matter continuously, the strong coupling of the system should satisfy two conditions, namely $g_{PX} > \frac{|\hbar\Gamma_P - \hbar\Gamma_X|}{2} = \frac{|33.42 - 16.05|}{2} =$ 8.68 meV, and $g_{PX} > \sqrt{\frac{1}{2}(\hbar\Gamma_P)^2 + \frac{1}{2}(\hbar\Gamma_X)^2} = \sqrt{\frac{1}{2}(33.42)^2 + \frac{1}{2}(16.05)^2} = 26.21$ meV. As a result, the calculated values reveal for being the Rabi splitting of the system is nonvanishing and can be experimentally measured[34]. Besides, we have calculated the coupling strength between the plasmon mode of the Au cavity and the excitons of WSe_2 monolayer and enter the strong coupling regime. The Au-WSe_2 nanostructure resulted in a Rabi splitting of 77.86 meV and a coupling strength of 47.08 meV at the detuning of Fig. 3(c).

Analogous to Au-$MoSe_2$ nanostructure, the calculated Rabi splitting of Au-WSe_2 nanostructure is nonvanishing and can be observed experimentally. Here, to verify that the system is nonvanishing, we substituted the HWHM of the uncoupled plasmon and WSe_2 exciton modes with $\hbar\Gamma_P = 44.64$ meV and $\hbar\Gamma_X = 7.745$ meV. The fitted data of the UPB and LPBs in Fig. 3(a) and 3(c) are matched well with the absorption mapping of Au-$MoSe_2$ and Au-WSe_2 in Fig. 2(b) and 2(e), respectively.

The geometry of the Au nanostructures influences the Rabi splitting of Au-WSe_2 heterostructures. Figure 4(d) and 4(e) illustrate the Rabi splitting Au-WSe_2 decreases with increasing thickness and cavity gap of Au nanostructure. This variation may be attributed to changes in the skin depth of the plasmonic Au cavity. The skin depth of the Au cavity is estimated as the point where the Rabi splitting of Au-WSe_2 nanostructures saturates, at which the incident electric field ($\boldsymbol{E}_0$) can be decreased by a value of 1/e. Hence, the electric field travelled inside the gold film to a certain distance of $\frac{1}{e}|\boldsymbol{E}_0|$ is called skin depth (δ), is given by $\delta = \sqrt{\frac{2}{\omega\mu\sigma}}$, where σ is the conductivity of gold with $\sigma_{Au} = 4.1 \times 10^7$ Siemens/meter (S/m), ω is angular frequency of the incident electromagnetic wave ($\omega = 2\pi f$), and μ magnetic permeability of gold, $\mu_{Au} \sim \mu_0 = 4\pi \times 10^{-7}$ Henry/meter (H/m)[38]. The frequency was set to the resonance frequency of the plasmon oscillation of the uncoupled Au cavity, assumed to match the frequency of the incident light (see Fig. 4(f)). As a result, the calculated skin depth (δ) for a thickness of 80 nm at a cavity gap of 39 nm is 3.80 nm, and for a thickness of 90 nm at a cavity gap of 42 nm is 3.82 nm. So, the electromagnetic fields that can penetrate are almost saturated at these points and result in similar Rabi splitting with their corresponding larger size and wider cavity gap (see Fig. 4(d) and 4(e)). Furthermore, the skin depth of electromagnetic waves in the Au cavity decreases as the thickness of the nanostructure decreases due to increased scattering and interactions at the surfaces. This leads to higher confinement and larger Rabi splitting, which is consistent with our results. As can be seen from Fig. 4(b), the Au cavity with a thickness of 50 nm has higher near-field enhancement than its corresponding with 90 nm. It is worth mentioning that the hybrid nanostructure of Au-WSe_2 revealed in Fig. 4(c) resulted an $|\boldsymbol{E}/\boldsymbol{E}_0|$ of 118 compared to that of Au cavity with 28. Therefore, plasmon-exciton coupling with a small gold skin depth promotes the formation of hybridized states and stronger coupling.

In addition to investigating the effect of the thickness of the Au cavity on the strong coupling of Au-WSe_2 heterostructure, we examined the impact of the cavity gap at a fixed thickness. Specifically, we considered an uncoupled Au cavity thickness of t = 90 nm while varying the other parameters (W_1 = 22–58 nm, W_2 = 16–52 nm, g = 98.5–116.5 nm, α = 290–326 nm, and h = 148.5–166.5 nm). Figures S6(b) and S6(c) showed that altering the cavity gap of the Au nanostructure resulted in a tunable plasmon resonance that could match with excitons of uncoupled WSe_2. Furthermore, Fig. S6(b) revealed a significant redshift in the absorption spectrum with a decreasing cavity gap, indicating the presence of strong plasmon coupling[20,32]. Figure 4(b) and 4(c)

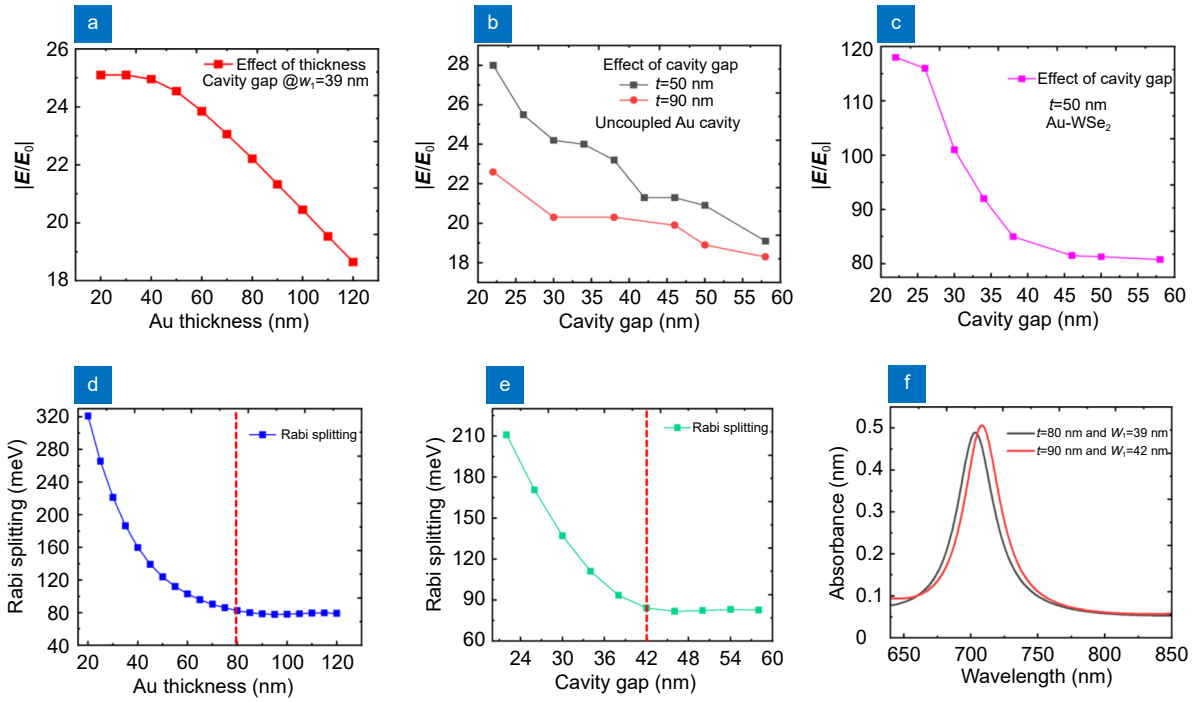

Fig. 4 | Size and cavity gap–dependent electric field enhancement and Rabi splitting. (**a**) Calculated electric field enhancement by increasing the size of the Au nanostructure from 20 to 120 nm. (**b**) Calculated near-field enhancements of the uncoupled Au cavity as a function of cavity gap distance with a fixed thickness of t = 50 nm and 90 nm. The calculated near-field enhancement distributions $|\boldsymbol{E}/\boldsymbol{E}_0|$ of the Au cavity are size-dependent. (**c**) Calculated near-field enhancements of the Au-WSe_2 heterostructure as a function of cavity gap with a thickness of t = 50 nm. Compared to the uncoupled Au cavity with a thickness of t = 50 nm and a cavity gap of W_1 = 22 nm, the Au-WSe_2 heterostructure demonstrates higher near-field enhancement. Their calculated electric field profile and its corresponding catenary-shaped near-field enhancement revealed that the narrower cavity gap has higher field confinement (see Fig. S5 in the Supplementary information). (**d**) Size-dependent Rabi splitting of Au-WSe_2 while the period and cavity gap are fixed at 420 nm, W_1 = 39 nm, and W_2 = 33 nm. (**e**) Cavity gap-dependent Rabi splitting of Au-WSe_2 while the period and thickness of Au cavity are fixed at 420 nm and 90 nm, respectively. (**f**) Plasmon resonance of uncoupled Au cavity corresponds to t = 80 nm at cavity gap of W_1 = 39 nm and t = 90 nm at cavity gap of W_1 = 42 nm, respectively. Their corresponding plasmon resonance frequency is 426.08 THz, and 423.1 THz, respectively.

confirmed that a cavity gap of W_1 = 22 nm has a higher near-field enhancement than that of W_1 = 58 nm (see Fig. S5(a–d) in the Supplementary information). The catenary-shaped field enhancement scales the plasmon coupling and its corresponding strong plasmon-exciton coupling. As seen in Fig. 4(e), the Rabi splitting of the Au-WSe_2 heterostructure decreases from 211 to 82.7 meV with an increasing cavity gap distance (W_1) from 22 to 58 nm. Both Rabi splitting and near-field enhancement of Au-WSe_2 consistently decreased with an increasing cavity gap (see Fig. 4(c) and S5(d)). Increasing the cavity gap distance leads to lower confinement. It's important to note that the Rabi splitting shown in Fig. 4(e) is extracted from Fig. 5(d) shows two different hybridized modes resulting from the cavity-gap-dependent strong coupling of Au-WSe_2. Increasing the cavity gap caused the lower branch to gradually shift to higher energy wavelengths and cross the excitons of WSe_2, which depicts the strong coupling regime (see Fig. S7(b) in the Supplementary information).

To further validate the effect of the cavity gap on near-field coupling, we demonstrated an Ag cavity with a thickness of 50 nm. The calculated catenary-shaped optical fields decrease with increasing cavity gap distance (see Fig. S8(a–c) in the Supplementary information). The calculated catenary-shaped field enhancement of the Ag cavity is broadly similar to that of its corresponding Au cavity. Varying the cavity gap (W_1) from 22 to 58 nm lowered the $|\boldsymbol{E}/\boldsymbol{E}_0|$ from 59.6 to 27.6.

Moreover, in investigations of strong plasmon-exciton coupling, the plasmonic cavity's quality factor (Q-factor) plays a significant role by confining photons inside the cavity. G Zengin et al. calculated a Q-factor of 20.2 for single isolated silver nanoprisms, which were applied in strong plasmon-exciton coupling under ambient conditions[37]. In contrast, the introduced plasmonic

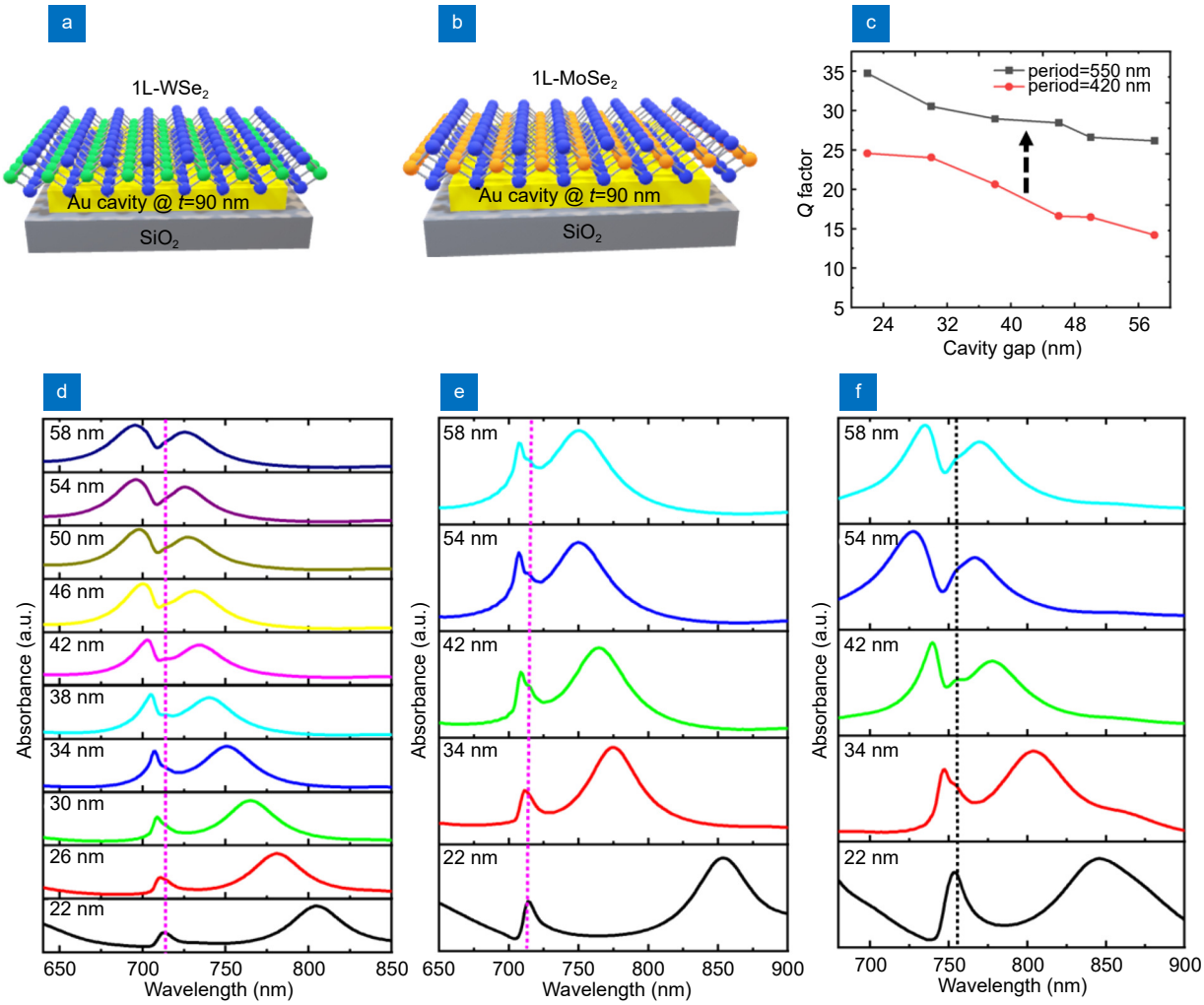

Fig. 5 | Effect of Cavity gap on strong coupling of Au-WSe_2 and Au-$MoSe_2$ on the substrate. Schematic drawing of (**a**) Au-WSe_2, and (**b**) Au-$MoSe_2$ nanostructures on SiO_2 substrate. (**c**) Quality factors (*Q*) as a function of period and cavity gap of gold nanostructure at a thickness of 90 nm. (**d**) Normal-incidence absorption spectra of the WSe_2 monolayer directly embedded in the Au cavity with different cavity gaps. Strong coupling of (**e**) Au-WSe_2, and (**f**) Au-$MoSe_2$ on SiO_2 substrate as a function of Au cavity gap. Here, the diameter of the Au cavity is 90 nm, while the cavity gap varies from 22 nm to 58 nm. The purple and black dash lines represent the excitons of WSe_2 and $MoSe_2$, respectively.

metamaterial Au cavity possesses a higher Q-factor, approximately 35, due to the increased confinement of near-field enhancement within the cavity (see Fig. 5(c)). The higher *Q* factor ~35 means that the plasmon survives in the cavity for 35 cycles before dephasing, leading to lower energy losses and intensifying the strength of plasmon-exciton coupling. Moreover, these plasmonic cavities can be easily hybridized with photonic cavities to enhance the performance of advanced quantum technologies[39].

In addition, we investigated the effect of the substrate on the Rabi splitting of Au-$MoSe_2$ and Au-WSe_2 nanostructures (see Fig. 5(a) and 5(b) for the design). To examine the substrate's impact on Rabi splitting, we used SiO_2 with a refractive index of 1.45, while adjusting the Au cavity gap (W_1) from 22 nm to 58 nm, with a fixed thickness of t = 90 nm. Figure 5(e) and 5(f) reveal that nanostructures with a cavity gap of 22 nm exhibit a higher energy splitting of the UPB and LPB than those with a 58 nm gap. Besides, Fig. 5(e) shows that the LPB of Au-WSe_2/SiO_2 has shifted to a lower energy level compared to Au-WSe_2 in the air (see Fig. 5(d)), which is expected to induce a redshift in the plasmon resonance due to the dielectric screening effect[40]. As seen in Fig. 5(e) and 5(f), both Au-WSe_2 and Au-$MoSe_2$ on the substrate cross the energy levels of excitons, which is crucial for further experimental fabrication and practical applications. This is because the plasmonic resonance of the Au cavity has higher confinement with a small mode volume, inducing faster energy exchange in the plexcitons.

Table 1 | Shows the Rabi splitting of plasmonic metal nanocavities with excitons in TMDCs. To align the uncoupled Ag plasmon resonances with TMDC excitons, we varied the period of the cavity slits while keeping the Ag thickness fixed at 50 nm. For additional geometric parameters of the hybrid nanostructures of Ag-WSe_2 and Ag-WS_2, please refer to Fig. S9(a) in the Supplementary information.

Excitonic TMDC (monolayer)	Previous studies			Rabi-splitting in our work [meV]
	Hybrid structure	Rabi splitting in [meV]	Ref.	
$MoSe_2$	$MoSe_2$ Monolayer withgold bowtie nanoantenna	130	ref.[43]	
	Au cavity−$MoSe_2$ monolayer		–	84−253.6
WS_2	Ag cavity−WS_2 monolayer		–	95.5
	Individual plasmonic gold nanorod on WS_2 monolayer	106	ref.[44]	
	Single Au@Ag nanocavity and WS_2 monolayer	110	ref.[45]	
WSe_2	Single silver nanorod on WSe_2 monolayer	49.5	ref.[11]	
	Ag cavity−WSe_2 monolayer		–	97.7
	Plasmonic nanocavities−WSe_2 (i.e., detuning is shown with 7 layers of WSe_2)	135	ref.[46]	
	Au cavity−WSe_2 monolayer		–	77.86−320

Finally, we compare the feasibility and performance of our plasmonic metamaterial cavity structure with those of previously reported plasmonic modes based on individual plasmonic nanoantennas. Table 1 briefly compares Rabi splitting in plasmon-exciton hybrid nanostructures from previous studies to our work. In addition to investigating strong coupling in Au-$MoSe_2$ and Au-WSe_2 heterostructures, we also calculated the Rabi splitting for Ag-WSe_2 and Ag-WS_2. To align the plasmon resonance induced by Ag metamaterial cavities with the excitons of WS_2 and WSe_2, we varied the period and cavity gap (see Fig. S9(a) and S9(b) in the Supplementary information). Here, variations in the nanostructure's cavity gap and/or thickness can result in different Rabi splitting values (see Fig. 4(d) and 4(e)). Thus, increasing cavity gap distance weakens the near-field interaction between the surface plasmons and excitons in TMDC, thereby reducing the coupling strength (see Fig. 4(e)). On top of that, it's worth mentioning that the currently necessity of higher field confinement[41]. This strong confinement leads to more intense light-matter interactions. Additionally, unlike vertical nano-resonators, the electromagnetic field in metamaterial cavities can be aligned with the orientation dipole moment of TMDCs[33]. This alignment facilitates efficient energy transfer between the cavity's plasmons and the TMDC monolayers' excitons, resulting in significant Rabi-splitting.

Lastly, it is noteworthy to explain the practical feasibility of our design. Such a metal-TMDCs hybrid structure can be fabricated using a standard nanofabrication facility. Firstly, the metamaterial structures can be fabricated by depositing a thin gold or silver film on a glass substrate. After the film is prepared, focused ion beam (FIB) milling can be employed to etch the film to a certain depth[32]. Then, the thin film TMDC monolayer is transferred onto the Au/Ag cavity[42]. The strong coupling in the hybrid system can be confirmed by measuring it using photoluminescence measurements[33].

Conclusion

In summary, we have successfully demonstrated that the catenary-shaped near-field enhancement of metallic metamaterial cavities results in a large Rabi splitting under ambient conditions. By tuning the size of the cavity gap and thickness of the plasmonic Ag/Au cavities, anticrossing behavior of the plasmon-exciton polaritonic hybrid states (Plexciton) with a Rabi splitting ranging from 77.86 to 320 meV is observed. The resulting Plexcitons are analyzed using Hopfield coefficients, which can be calculated using a two-coupled oscillator model. The calculated Rabi splitting for the Au-WSe_2 and Au-$MoSe_2$ nanostructures is nonvanishing and can be experimentally measured. The results obtained in our study and the proposed plasmonic metamaterial cavity, along with its heterostructures, will pave the way for improving our understanding of the effect of catenary-shaped optical fields on strong plasmon−exciton coupling. The plasmonic Au cavity has a quality factor of ~35, and its heterostructures have the potential to enable the realization of a single-photon emitter. Besides, the enhanced interaction between the plasmon-excitons leads to the realization of compact and low-threshold lasers, as well as the advancement of optoelectronic devices.

References

1. Deng F, Liu HF, Xu L, Lan S, Miroshnichenko AE. Strong exciton–plasmon coupling in a WS_2 monolayer on Au film hybrid structures mediated by liquid Ga nanoparticles. *Laser Photonics Rev* **14**, 1900420 (2020).
2. Liu F, Brash AJ, O'Hara J, Martins LMPP, Phillips CL et al. High purcell factor generation of indistinguishable on-chip single photons. *Nat Nanotechnol* **13**, 835–840 (2018).
3. Santhosh K, Bitton O, Chuntonov L, Haran G. Vacuum Rabi splitting in a plasmonic cavity at the single quantum emitter limit. *Nat Commun* **7**, 11823 (2016).
4. Degen CL, Reinhard F, Cappellaro P. Quantum sensing. *Rev Mod Phys* **89**, 035002 (2017).
5. Wang SJ, Li SL, Chervy T, Shalabney A, Azzini S et al. Coherent coupling of WS_2 monolayers with metallic photonic nanostructures at room temperature. *Nano Lett* **16**, 4368–4374 (2016).
6. Brongersma ML, Shalaev VM. The case for plasmonics. *Science* **328**, 440–441 (2010).
7. Baumberg JJ, Aizpurua J, Mikkelsen MH, Smith DR. Extreme nanophotonics from ultrathin metallic gaps. *Nat Mater* **18**, 668–678 (2019).
8. Törmä P, Barnes WL. Strong coupling between surface plasmon polaritons and emitters: a review. *Rep Prog Phys* **78**, 013901 (2014).
9. Vasa P, Wang W, Pomraenke R, Lammers M, Maiuri M et al. Real-time observation of ultrafast Rabi oscillations between excitons and plasmons in metal nanostructures with J-aggregates. *Nat Photonics* **7**, 128–132 (2013).
10. Chikkaraddy R, De Nijs B, Benz F, Barrow SJ, Scherman OA et al. Single-molecule strong coupling at room temperature in plasmonic nanocavities. *Nature* **535**, 127–130 (2016).
11. Zheng D, Zhang SP, Deng Q, Kang M, Nordlander P et al. Manipulating coherent plasmon–exciton interaction in a single silver nanorod on monolayer WSe_2. *Nano Lett* **17**, 3809–3814 (2017).
12. Li BW, Zu S, Zhang ZP, Zheng LH, Jiang Q et al. Large Rabi splitting obtained in Ag-WS_2 strong-coupling heterostructure with optical microcavity at room temperature. *Opto - Electron Adv* **2**, 190008 (2019).
13. Huang LJ, Krasnok A, Alú A, Yu YL, Neshev D et al. Enhanced light–matter interaction in two-dimensional transition metal dichalcogenides. *Rep Prog Phys* **85**, 046401 (2022).
14. Rahaman M, Kim G, Ma KY, Song S, Shin HS et al. Tailoring exciton dynamics in TMDC heterobilayers in the ultranarrow gap-plasmon regime. *npj 2D Mater Appl* **7**, 66 (2023).
15. Qin MB, Duan JY, Xiao SY, Liu WX, Yu TB et al. Manipulating strong coupling between exciton and quasibound states in the continuum resonance. *Phys Rev B* **105**, 195425 (2022).
16. Jiang YZ, Wang H, Wen SY, Chen HJ, Deng SZ. Resonance coupling in an individual gold nanorod–monolayer WS_2 heterostructure: photoluminescence enhancement with spectral broadening. *ACS Nano* **14**, 13841–13851 (2020).
17. Al-Ani IAM, As'ham K, Klochan O, Hattori HT, Huang LJ et al. Recent advances on strong light-matter coupling in atomically thin TMDC semiconductor materials. *J Opt* **24**, 053001 (2022).
18. Han XB, Wang K, Xing XY, Wang MY, Lu PX. Rabi splitting in a plasmonic nanocavity coupled to a WS_2 monolayer at room temperature. *ACS Photonics* **5**, 3970–3976 (2018).
19. Kawata S. *Near-Field Optics and Surface Plasmon Polaritons* (Springer, Berlin Heidelberg, 2001).
20. Ma XL, Guo YH, Pu MB, Li X, Luo XG. Refined model for plasmon ruler based on catenary-shaped optical fields. *Plasmonics* **14**, 845–850 (2019).
21. Luo XG. *Catenary Optics* (Springer, Singapore, 2019).
22. Huang YJ, Luo J, Pu MB, Guo YH, Zhao ZY et al. Catenary electromagnetics for ultra - broadband lightweight absorbers and large - scale flat antennas. *Adv Sci* **6**, 1801691 (2019).
23. Xie X, Pu MB, Huang YJ, Ma XL, Li X et al. Heat resisting metallic meta - skin for simultaneous microwave broadband scattering and infrared invisibility based on catenary optical field. *Adv Mater Technol* **4**, 1800612 (2019).
24. Cao E, Lin WH, Sun MT, Liang WJ, Song YZ. Exciton-plasmon coupling interactions: from principle to applications. *Nanophotonics* **7**, 145–167 (2018).
25. Gong MG, Jiang D, Tao T, Chen F, Xu CX et al. Surface plasmon coupling regulated $CsPbBr_3$ perovskite lasers in a metal–insulator–semiconductor structure. *RSC Adv* **11**, 37218–37224 (2021).
26. Lee B, Liu WJ, Naylor CH, Park J, Malek SC et al. Electrical tuning of exciton–plasmon polariton coupling in monolayer MoS_2 integrated with plasmonic nanoantenna lattice. *Nano Lett* **17**, 4541–4547 (2017).
27. Kim JH, Lee J, Kim H, Yun SJ, Kim J et al. Optical logic operation via plasmon-exciton interconversion in 2D semiconductors. *Sci Rep* **9**, 9164 (2019).
28. Qian ZY, Ren JJ, Zhang F, Duan XK, Gong QH et al. Nanoscale quantum plasmon sensing based on strong photon–exciton coupling. *Nanotechnology* **31**, 125001 (2020).
29. Zhang L, Gogna R, Burg W, Tutuc E, Deng H. Photonic-crystal exciton-polaritons in monolayer semiconductors. *Nat Commun* **9**, 713 (2018).
30. Al - Ani IAM, As'ham K, Huang LJ, Miroshnichenko AE, Hattori HT. Enhanced strong coupling of TMDC monolayers by bound state in the continuum. *Laser Photonics Rev* **15**, 2100240 (2021).
31. Johnson PB, Christy RW. Optical constants of the noble metals. *Phys Rev B* **6**, 4370–4379 (1972).
32. Bouloumis TD, Kotsifaki DG, Nic Chormaic S. Enabling self-induced back-action trapping of gold nanoparticles in metamaterial plasmonic tweezers. *Nano Lett* **23**, 4723–4731 (2023).
33. Zhang M, Tian Y, Chen XZ, Sun Z, Zhu XL et al. Observation of ultra-large Rabi splitting in the plasmon-exciton polaritons at room temperature. *Nanophotonics* **12**, 3267–3275 (2023).
34. As'ham K, Al-Ani I, Huang LJ, Miroshnichenko AE, Hattori HT. Boosting strong coupling in a hybrid WSe_2 monolayer–anapole–plasmon system. *ACS Photonics* **8**, 489–496 (2021).
35. As'ham K, Al-Ani I, Alaloul M, Abdo S, Abdulghani A et al. Enhanced strong coupling in the hybrid dielectric-metallic nanoresonator and WS_2 monolayer. *Phys Rev Appl* **19**, 054049 (2023).
36. Gao CG, You SJ, Zhang Y, Zhou CB, Xie Q. Strong coupling of excitons and electric/magnetic toroidal dipole modes in perovskite metasurfaces. *Opt Express* **31**, 34143–34153 (2023).
37. Zengin G, Wersäll M, Nilsson S, Antosiewicz TJ, Käll M et al. Realizing strong light-matter interactions between single-nanoparticle plasmons and molecular excitons at ambient conditions. *Phys Rev Lett* **114**, 157401 (2015).
38. Hassan SG, Mohammad EJ. Study of the skin depth in different

metallic atoms. *Mater Today Proc* **42**, 2749–2751 (2021).
39. Lu YW, Zhou WJ, Li Y, Li R, Liu JF et al. Unveiling atom-photon quasi-bound states in hybrid plasmonic-photonic cavity. *Nanophotonics* **11**, 3307–3317 (2022).
40. Xu G, Tazawa M, Jin P, Nakao S, Yoshimura K. Wavelength tuning of surface plasmon resonance using dielectric layers on silver island films. *Appl Phys Lett* **82**, 3811–3813 (2003).
41. Ai RQ, Xia XY, Zhang H, Chui KK, Wang JF. Orientation-dependent interaction between the magnetic plasmons in gold nanocups and the excitons in WS_2 monolayer and multilayer. *ACS Nano* **17**, 2356–2367 (2023).
42. Gurarslan A, Yu YF, Su LQ, Yu YL, Suarez F et al. Surface-energy-assisted perfect transfer of centimeter-scale monolayer and few-layer MoS_2 films onto arbitrary substrates. *ACS Nano* **8**, 11522–11528 (2014).
43. Petrić MM, Kremser M, Barbone M, Nolinder A, Lyamkina A et al. Tuning the optical properties of a $MoSe_2$ monolayer using nanoscale plasmonic antennas. *Nano Lett* **22**, 561–569 (2022).
44. Wen JX, Wang H, Wang WL, Deng ZX, Zhuang C et al. Room-temperature strong light–matter interaction with active control in single plasmonic nanorod coupled with two-dimensional atomic crystals. *Nano Lett* **17**, 4689–4697 (2017).
45. Liang K, Jin L, Deng XY, Jiang P, Yu L. Fine-tuning biexcitons-plasmon coherent states in a single nanocavity. *Nanophotonics* **12**, 3471–3480 (2023).
46. Kleemann ME, Chikkaraddy R, Alexeev EM, Kos D, Carnegie C et al. Strong-coupling of WSe_2 in ultra-compact plasmonic nanocavities at room temperature. *Nat Commun* **8**, 1296 (2017).

Acknowledgements

This work is supported by the Australian Research Council (DP200101353).

Competing interests

The authors declare no competing financial interests.

Supplementary information

Supplementary information for this paper is available at https://doi.org/10.29026/oea.2024.230181